



# Sensitivity impacts owing to the variations in the type of zero-range pairing forces on the fission properties using the density functional theory

Yang Su<sup>1</sup> · Ze-Yu Li<sup>1</sup> · Li-Le Liu<sup>1</sup> · Guo-Xiang Dong<sup>2</sup> · Xiao-Bao Wang<sup>2</sup> · Yong-Jing Chen<sup>1</sup>

Received: 17 October 2023 / Revised: 10 January 2024 / Accepted: 11 January 2024 / Published online: 3 May 2024

© The Author(s), under exclusive licence to China Science Publishing & Media Ltd. (Science Press), Shanghai Institute of Applied Physics, the Chinese Academy of Sciences, Chinese Nuclear Society 2024

## Abstract

Using the Skyrme density functional theory, potential energy surfaces of  $^{240}\text{Pu}$  with constraints on the axial quadrupole and octupole deformations ( $q_{20}$  and  $q_{30}$ ) were calculated. The volume-like and surface-like pairing forces, as well as a combination of these two forces, were used for the Hartree–Fock–Bogoliubov approximation. Variations in the least-energy fission path, fission barrier, pairing energy, total kinetic energy, scission line, and mass distribution of the fission fragments based on the different forms of the pairing forces were analyzed and discussed. The fission dynamics were studied based on the time-dependent generator coordinate method plus the Gaussian overlap approximation. The results demonstrated a sensitivity of the mass and charge distributions of the fission fragments on the form of the pairing force. Based on the investigation of the neutron-induced fission of  $^{239}\text{Pu}$ , among the volume, mixed, and surface pairing forces, the mixed pairing force presented a good reproduction of the experimental data.

**Keywords** Nuclear fission · Density functional theory · Pairing force · Potential energy surfaces · Fission fragment distribution

## 1 Introduction

Nuclear fission, i.e., the phenomenon that one (usually heavy) atomic nucleus may separate into two or more fragments, has been discovered for more than eighty years [1, 2]. It is accompanied by the release of abundant energy [3] and has a wide range of applications. In addition to the important applications in energy and production of rare isotopes, fission also plays a crucial role in fundamental physics, such as synthesizing superheavy elements [4–6], as well

as constraints on the r-process in neutron-star mergers [7]. Therefore, several theoretical approaches have been utilized to describe the fission process and observations [8–17]. As shown in Ref. [8], the microscopic models that were applied to fission thus far utilize the density functional theory (DFT), which is based on effective nucleon–nucleon interactions.

As one of the dominant residual correlations in the atomic nuclei, the pairing interaction is critical for understanding the fission process. Extensive studies regarding the influence of pairing interactions on the fission properties were performed, such as the effect on the fission barrier heights, fission isomer excitation energies, and collective inertia [18–23]. In Ref. [20], the fission dynamic calculation based on the covariant DFT was performed for the fission of  $^{226}\text{Th}$ , in which both the symmetric and asymmetric fission modes coexist. The asymmetric fission mode dominated as the pairing force decreased, whereas the symmetric fission mode dominated as the pairing force increased. The time-dependent superfluid local density approximation (TDSLDA) method has demonstrated that fission significantly accelerates as the pairing force increases [24]. The

---

This work was supported by the National Key R & D Program of China (No. 2022YFA1602000), National Natural Science Foundation of China (Nos. 12275081, U2067205, 11790325, and U1732138), and the Continuous-support Basic Scientific Research Project.

---

✉ Xiao-Bao Wang  
xbwang@zjhu.edu.cn

<sup>1</sup> China Nuclear Data Center, China Institute of Atomic Energy, Beijing 102413, China

<sup>2</sup> School of Science, Huzhou University, Huzhou 313000, China

effect of the dynamic pairing correlations on the fission process was studied in Refs. [25, 26].

In our previous work, the role of the pairing force on the static fission properties and fission dynamic process was studied [22, 27–29], which demonstrated that the variation in the strength of the pairing correlation can significantly influence the fission process. However, whether the form of pairing force can also impact the fission properties is noteworthy. A schematic pairing force was originally introduced in [30], and parameters of the density-dependent pairing correlation were studied in Refs. [31–33]. Specifically, considering Skyrme DFT, different types of pairing forces have been used for studying the nuclear structure, such as the volume-like, surface-like, and mixed-type pairing forces. In Refs. [34–36], various types of the pairing interactions (volume-, surface-, and mixed-type pairing forces) were used to study the pairing gaps in even–even nuclei over the entire nuclear chart, the odd–even staggering behavior of binding energies around tin isotopes, and to predict the two-neutron separation energies and neutron pairing gaps [36]. In this study, whether the form of the pairing force can influence the static aspects of the fission properties and dynamics was investigated. The fission process of  $^{240}\text{Pu}$  was studied in Skyrme DFT and the time-dependent generator coordinate method (TDGCM) plus Gaussian overlap approximation (GOA) (TDGCM + GOA) framework.

In Sect. 2, we briefly describe the main features of the theoretical approach. Details regarding the calculated results for the least-energy fission path, fission barrier, pairing energy, total kinetic energy, scission line, and mass distribution of fission fragments using various types of pairing forces are analyzed and discussed in Sect. 3. Finally, Sect. 4 presents a summary of the principal results.

## 2 Theoretical framework

Skyrme DFT was applied as the microscopic method to study the static fission properties and prepare the input files for the dynamic calculation. The dynamic process was further investigated in the framework of TDGCM. Thus, in this section, these two methods are briefly explained. Detailed formulations of the Skyrme DFT can be found in Ref. [37], and those of TDGCM can be found in Refs. [38–40].

### 2.1 Density functional theory approach for the description of PES

For the local density approximation of DFT, the total energy of the finite nuclei can be calculated using the space integral of the Hamiltonian density  $\mathcal{H}(\mathbf{r})$ , which consists of the kinetic energy  $\tau$ , potential energy  $\chi_t$ , and pairing energy  $\check{\chi}_t$  densities:

$$\mathcal{H}(\mathbf{r}) = \frac{\hbar^2}{2m} \tau(\mathbf{r}) + \sum_{t=0,1} \chi_t(\mathbf{r}) + \sum_{t=0,1} \check{\chi}_t(\mathbf{r}). \quad (1)$$

Here,  $\tau(\mathbf{r})$  is the density of the kinetic energy, and the symbol  $t = 0, 1$  indicates the isoscalar or isovector, respectively [41].

The mean-field potential energy in the Skyrme DFT usually has the following form:

$$\begin{aligned} \chi_t(\mathbf{r}) = & C_t^{\rho\rho} \rho_t^2 + C_t^{\rho\tau} \rho_t \tau_t + C_t^J \mathbb{J}_t^2 \\ & + C_t^{\rho\Delta\rho} \rho_t \Delta\rho_t + C_t^{\rho\nabla J} \rho_t \nabla \cdot \mathbf{J}_t. \end{aligned} \quad (2)$$

Here, the particle density  $\rho_t$ , kinetic density  $\tau_t$ , and spin current vector densities  $\mathbf{J}_t$  ( $t = 0, 1$ ) can be obtained from the density matrix  $\rho_t(\mathbf{r}\sigma, \mathbf{r}'\sigma')$ , depending on the spatial ( $\mathbf{r}$ ) and spin ( $\sigma$ ) coordinates. In the aforementioned formula,  $C_t^{\rho\rho}$ ,  $C_t^{\rho\tau}$ , and *etc.* are the coupling constants in the Hamiltonian density  $\mathcal{H}(\mathbf{r})$ , corresponding to the different types of densities, most of which are real numbers;  $C_t^{\rho\rho} = C_{t0}^{\rho\rho} + C_{tD}^{\rho\rho} \rho_0^\gamma$  is an exception, which is the traditional density-dependent term. Expressions relating the coupling constants to the standard Skyrme parameters can be found in Ref. [42]. Specifically, the spin–orbit interaction in the Skyrme force corresponds to the term  $C_t^{\rho\nabla J} \rho_t \nabla \cdot \mathbf{J}_t$ .

In the DFT, the pairing correlation is usually incorporated by the Hartree–Fock–Bogoliubov (HFB) method [37]. For the Skyrme energy density functional, a commonly used pairing force is the density-dependent, zero-range potential, which can be expressed as follows: Refs. [8, 43]:

$$\hat{V}_{\text{pair}}(\mathbf{r}, \mathbf{r}') = V_0^{(n,p)} \left[ 1 - \eta \left( \frac{\rho(\mathbf{r})}{\rho_0} \right)^\gamma \right] \delta(\mathbf{r} - \mathbf{r}'). \quad (3)$$

Here,  $V_0^{(n,p)}$  is the pairing strength for neutrons (n) and protons (p), and the exponent  $\gamma$  of the density dependence affects the appearance of the neutron skins and halos [44], for which  $\gamma = 1$  is widely used [45, 46].  $\rho_0$  is the average density inside the nucleus (often considered as the saturation density of nuclear matter, and set as  $0.16 \text{ fm}^{-3}$ ), and  $\rho(\mathbf{r})$  is the total density. Different types of pairing forces can be obtained by choosing different values of  $\eta$ . The pairing force is “volume-like”, which indicates that if  $\eta = 0$ , there is no explicit density dependence. The pairing force acts equivalently inside the nuclear volume. In contrast, the pairing force will be “surface-like” for  $\eta = 1$ , which has a significant effect around the nuclear surface and a small impact in the center area of the nucleus. The choice of  $\eta = \frac{1}{2}$  is often called a mixed pairing force, which is the average of these two types of pairing forces. To test the sensitivities on the fission-related properties based on the form of the pairing force, we considered  $\eta = 0, 0.25, 0.5, 0.75$ , and  $1$ .  $\eta = 0.25$  and  $0.75$  were used for test purposes, and the

other choices of the  $\eta$  values have been frequently used for structural studies.

## 2.2 Time-dependent generator coordinate method for fission dynamics

Fission is a large-amplitude collective motion and can be described as a slow adiabatic process driven by a few collective degrees of freedom within the framework of TDGCM. In this approach, the many-body state wave function of the fissioning system can be expressed by the following generic form:

$$|\Psi(t)\rangle = \int_{\mathbf{q}} f(\mathbf{q}, t) |\Phi(\mathbf{q})\rangle d\mathbf{q}. \quad (4)$$

where  $|\Phi(\mathbf{q})\rangle$  consists of a set of known many-body wave functions parameterized by a vector of continuous variables  $\mathbf{q}$ . Each of these  $\mathbf{q}$  is a collective variable and is chosen based on the specific physics problem. The quadrupole moment  $\hat{Q}_{20}$  and octupole moment  $\hat{Q}_{30}$  are usually chosen as the collective variables for the fission study.  $f(\mathbf{q}, t)$  is the weighted function, which is solved by using the time-dependent Schrödinger-like equation in the space of the coordinates  $\mathbf{q}$ . Under the GOA, this equation can be expressed as follows:

$$i\hbar \frac{\partial g(\mathbf{q}, t)}{\partial t} = \hat{H}_{\text{coll}}(\mathbf{q})g(\mathbf{q}, t). \quad (5)$$

The collective Hamiltonian  $\hat{H}_{\text{coll}}(\mathbf{q})$  is as follows:

$$\hat{H}_{\text{coll}}(\mathbf{q}) = -\frac{\hbar^2}{2} \sum_{ij} \frac{\partial}{\partial q_i} B_{ij}(\mathbf{q}) \frac{\partial}{\partial q_j} + V(\mathbf{q}), \quad (6)$$

where  $V(\mathbf{q})$  is the collective potential, and the inertia tensor  $B_{ij}(\mathbf{q}) = \mathcal{M}^{-1}(\mathbf{q})$  is the inverse of the mass tensor  $\mathcal{M}$ . The potential and mass tensor are determined by the Skyrme DFT in this study.  $g(\mathbf{q}, t)$  is the complex collective wave function of the collective variables  $\mathbf{q}$  and contains all the information regarding the dynamic of the fission system.

For the description of fission, the collective space is divided into an inner region with a single nuclear density distribution and an external region that contains the two fission fragments. The scission contour defines the hyper-surface that separates the two regions. The flux of the probability current through this hyper-surface provides a measure of the probability of observing a given pair of fragments at time  $t$ . The integrated flux  $F(\xi, t)$  for the surface element  $\xi$  on the scission hyper-surface is calculated as follows:

$$F(\xi, t) = \int_{t=0}^t dt \int_{\mathbf{q} \in \xi} \mathbf{J}(\mathbf{q}, t) \cdot d\mathbf{S}, \quad (7)$$

as in Ref. [40], where  $\mathbf{J}(\mathbf{q}, t)$  is the current

$$\mathbf{J}(\mathbf{q}, t) = \frac{\hbar}{2i} B(\mathbf{q}) [g^*(\mathbf{q}, t) \nabla g(\mathbf{q}, t) - g(\mathbf{q}, t) \nabla g^*(\mathbf{q}, t)]. \quad (8)$$

The yield of the fission fragment with mass number  $A$  can be calculated as follows:

$$Y(A) = C \sum_{\xi \in \mathcal{A}} \lim_{t \rightarrow +\infty} F(\xi, t), \quad (9)$$

where  $\mathcal{A}$  indicates a set of all the surface elements  $\xi$  on the scission hyper-surface with a fragment mass of  $A$ , where  $C$  is the normalization constant to ensure that the total yield is normalized to 200 as usual. The yield of the fission fragment with the charge number  $Z$  can also be obtained from the integrated flux  $F(\xi, t)$ . The mass number  $A$  can be replaced with the charge number  $Z$  in Eq. 9; the summation is then over the set of all the  $\xi$  values on the scission frontier with the fragment charge number  $Z$ . In this study, the FELIX (version 2.0) [47] computer code was used for modeling the time evolution of the fissioning nucleus in the framework of TDGCM+GOA.

## 3 Results and discussion

The influence of the different types of pairing forces on the fission properties were studied based on Skyrme DFT with SkM\* parameters [48]. The DFT solvers HFBTHO(V3.00) [49] were used to calculate the potential energy surfaces (PESs). An axial symmetry was assumed. Thirty-one major shells of the axial harmonic-oscillator single-particle basis were used, and the number of the basis states was further truncated to be 1100. In this study, we considered five values of  $\eta$  (0, 0.25, 0.5, 0.75, and 1) in Eq. 3 as the different types of pairing forces. For each value of  $\eta$ , the pairing strength for the neutrons and protons was adjusted to reproduce a pairing gap of  $^{240}\text{Pu}$  extracted from the three-point formula of the odd-even mass staggering. A cutoff of 60 MeV was used as the pairing window in all the calculations.

Figure 1 presents the pairing strengths of the neutrons and protons for the pairing forces with different values of  $\eta$ . For  $\eta$  near 0, the pairing tends to occur equivalently in the nuclear volume. When it is near 1, the pairing tends to peak at the nuclear surface. For  $\eta$  between the values of 0.0 and 0.5, the absolute value of the pairing strength increased nearly linearly. However, for  $\eta = 1.00$ , there was a sudden increase in the pairing strength. The surface-like pairing force requires a significantly larger strength to produce the same pairing gap compared to the volume-like or mixed-type pairing forces. These results are consistent with previous studies. As demonstrated in Refs. [50, 51], the surface pairing force also has stronger strength than the volume and mixed pairing forces.

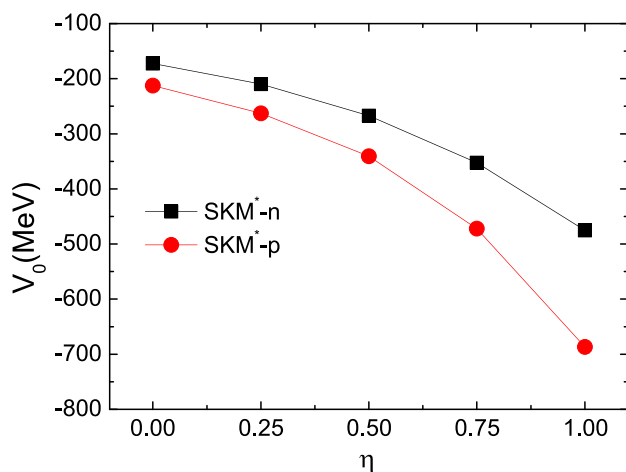


**Fig. 1** (color online) Pairing strength of the neutron (square) and proton (circle) as a function of the parameter  $\eta$ . The strength  $V_0$  was adjusted to reproduce the empirical pairing gaps in  $^{240}\text{Pu}$

### 3.1 Potential energy surface

As indicated in Sec. II.B, considering the adiabatic approximation approach for fission dynamics, obtaining the precise multidimensional PESs is the first step toward the dynamical description of fission. In this study, we chose the quadrupole moment ( $q_{20}$ ) and octupole moment ( $q_{30}$ ) as the collective parameters, which are the most important collective degrees of freedom for the nuclear fission study; they describe the elongation of the nucleus and mass asymmetry, respectively. Figure 2 presents the PESs of  $^{240}\text{Pu}$  calculated by using the HFB method with five different types of pairing forces ( $\eta = 0, 0.25, 0.5, 0.75,$  and  $1.0$ ) in the collective space of ( $q_{20}, q_{30}$ ). The collective variables ranged from 0 to 600 b for  $q_{20}$ , and from 0 to  $60 \text{ b}^{3/2}$  for  $q_{30}$  with the step of  $\Delta q_{20} = 2 \text{ b}$  and  $\Delta q_{30} = 2 \text{ b}^{3/2}$ .

As shown in Fig. 2, there is no notable difference in the topological properties of PESs with different types of pairing forces. Double-humped fission barriers were predicted for all the cases. An inner symmetric fission barrier followed by an outer asymmetric barrier was clearly distinguished. At  $q_{20} > 200 \text{ b}$ , symmetric valleys with large elongations were found. The symmetric and asymmetric fission valleys were well-separated by a ridge from  $(q_{20}, q_{30}) \approx (150 \text{ b}, 0 \text{ b}^{3/2})$  to  $(350 \text{ b}, 20 \text{ b}^{3/2})$ , and the height of the ridge gradually decreased as the  $\eta$  value increased. Therefore, the density-dependent surface pairing force led to the reduction of the ridge height. In addition, the asymmetric fission channel was favored for all the least-energy fission pathways, as indicated by the red lines in Fig. 2.

Energies of the symmetric and asymmetric fission paths as a function of the quadrupole moment ( $q_{20}$ ) are provided in Figs. 3a and b, respectively. The value of  $\eta$  varied from 0 to 1, indicating that the “volume-like” pairing force transitioned

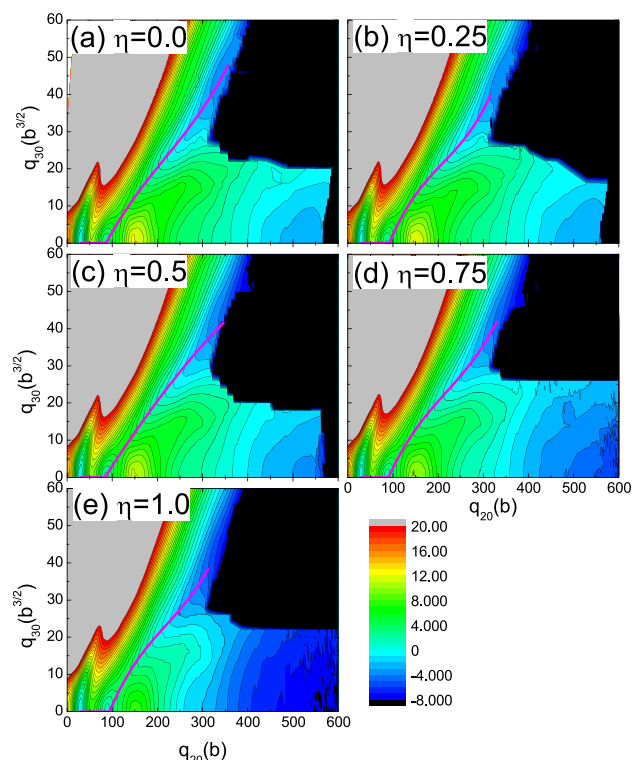


**Fig. 2** (color online) The PESs of  $^{240}\text{Pu}$  in the  $(q_{20}, q_{30})$  plane calculated with the SkM\*-DFT and the five different types of pairing forces in the HFB approximation. The value of  $\eta$  for the different types of pairing forces is provided in each panel. The energies are provided relative to the ground-state energy. The contours join the points on the surface with the same energy, and the interval of the contour is 1.0 MeV. The least-energy fission pathway is indicated by a solid red curve

into a surface pairing force. Figure 3 demonstrates that the fission barrier heights and isomeric-state energy decrease as  $\eta$  increases. Specifically, when  $\eta > 0.5$ , the fission barriers explicitly decrease. For the least-energy fission pathway shown in Fig. 3b, a smaller quadrupole moment is needed for the occurrence of the scission for a larger  $\eta$ .

Table 1 lists the energies of the ground state, isomeric states, and fission barrier heights for the different types of pairing forces, along with the corresponding quadrupole and octupole moments for each state. The energies of the isomeric state and heights of the fission barrier decrease as the  $\eta$  value increases. Owing to the lack of triaxial deformation in the collective space in our calculation, the heights of the fission barriers would be higher than those experimentally obtained, especially for the inner fission barrier [52, 53]. As indicated in the table, for  $\eta=1$ , the inner fission barrier height was near that demonstrated by the data, and the outer fission barrier was lower than that in the data, leaving no room for the triaxial degree of freedom. Thus,  $\eta=1$ , that is, the surface pairing force, may not be a good choice for the fission study. Based on

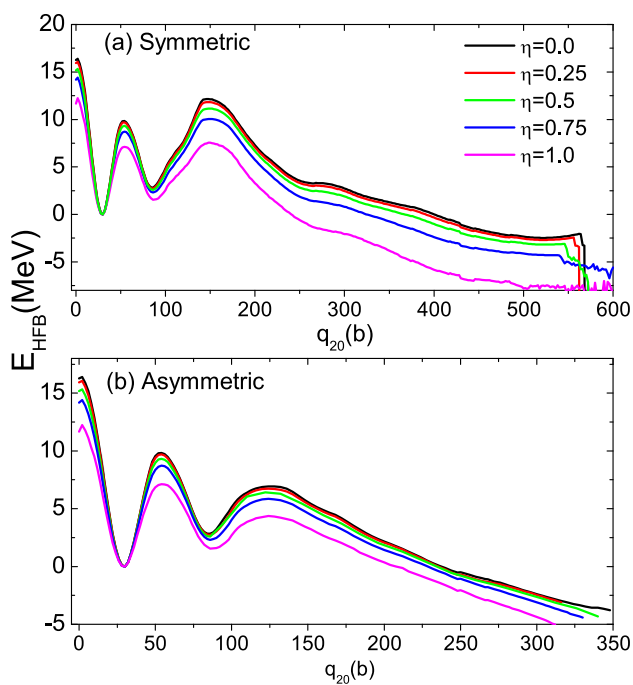


**Fig. 3** (color online) Energies along the symmetric and least-energy fission pathways in  $^{240}\text{Pu}$ , with different types of pairing correlations, are shown in panels (a) and (b), respectively. All these energies are relative to their ground-state values

Table 1, the deformations of these states, including the ground state, isomeric state, and inner and outer barriers, are generally not influenced by the type of pairing force. These deformations are mainly determined by the shell structure given by the mean-field potential. In our previous study [22], we also found that these deformations were relatively stable against the variations of the pairing strength.

**Table 1** Energies of the ground state, isomeric state, and fission barrier heights

		Ground state	Isomeric state	Inner barrier	Outer barrier
Energy (MeV)	Exp.	-1813.45 [54]	2.8 [55]	6.05* [56]	5.15* [56]
	0.0	-1805.06	2.83	9.83	6.90
	0.25	-1805.15	2.63	9.58	6.64
	0.5	-1805.35	2.59	9.32	6.46
	0.75	-1805.68	2.31	8.72	5.84
	1.0	-1806.44	1.55	7.12	4.36
Deformation ( $q_{20}/b, q_{30}/b^{3/2}$ )	0.0	(30,0)	(86,0)	(54,0)	(124,8)
	0.25	(30,0)	(86,0)	(54,0)	(124,8)
	0.5	(30,0)	(86,0)	(54,0)	(126,8)
	0.75	(30,0)	(86,0)	(54,0)	(124,8)
	0.75	(30,0)	(86,0)	(54,0)	(124,8)
	1.0	(30,0)	(86,0)	(54,0)	(124,8)

The empirical values are indicated by “\*”. The quadruple and octuple moments at the corresponding states are provided. The labels 0.0, 0.25, 0.5, 0.75, and 1.0 indicate different types of pairing forces and are the values of  $\eta$

### 3.2 Pairing energies

Figure 4 presents the pairing energies at different deformations for various types of pairing forces. The pairing energies at the ground and isomeric states are smaller than those at the fission barriers. At the same state, the pairing energy increases as the value of  $\eta$  increases, especially for  $\eta=1$ , which is the surface-type pairing force. The pairing gaps at different deformations are provided in Fig. 5. Once again, the pairing gap has a minimum at the ground state and a second minimum at the isomeric states. The pairing gaps are large around the fission barriers. For the adjustment of the strength of the different pairing forces used in this study, the same values of the pairing gaps in  $^{240}\text{Pu}$  were used. The figure demonstrates that at the smaller deformation region, the pairing gaps from the different types of pairing forces were relatively similar. However, when the deformation was large, explicit discrepancies appeared ( $q_{20} > 150$  b). For the pairing force with a smaller  $\eta$  value, the neutron and proton pairing gaps were generally smaller.

### 3.3 Mass tensor

The mass tensor  $\mathcal{M}$  reflects the response of the fissioning system to the collective coordinate changes. In this study, mass tensors were obtained from the static calculations by using the Skyrme DFT with the perturbative cranking approximation. As shown in Fig. 6, the elements of the mass tensor  $M_{22}$ ,  $M_{33}$ , and  $M_{23}$  were plotted as functions of  $q_{20}$  along the lowest-energy fission path for the different choices of  $\eta$ . The mass tensor given by ATDHFB was larger than that by GCM for all types of pairing forces. As indicated in Ref. [8], this was caused by the missing correlations in the GCM method. Generally, as the quadruple moments increase,  $M_{22}$  and  $M_{33}$  gradually decrease.  $M_{23}$  is

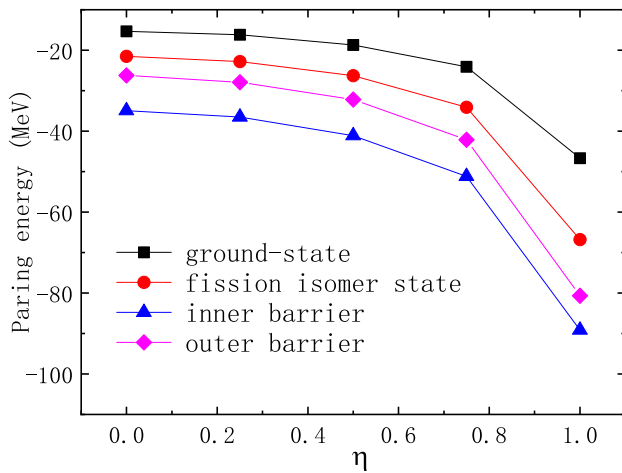


**Fig. 4** (color online) Pairing energy of the ground state, fission isomer state, and inner and outer fission barriers in  $^{240}\text{Pu}$  as a function of the  $\eta$  parameter in the pairing force

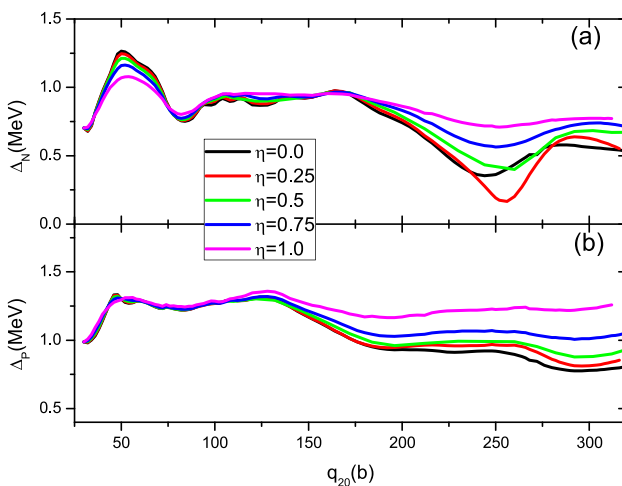


**Fig. 5** (color online) Pairing gap along the least-energy fission path for the neutron (a) and proton (b) with different types of pairing forces

negative, and its absolute value increases and has explicit fluctuations when the deformation is large. For different types of pairing forces tuned by  $\eta$ , the mass tensor apparently decreases and demonstrates reduced fluctuation against deformations when  $\eta$  is large. As indicated in Ref. [28], considering the mixed pairing force of  $\eta = 0.5$ , the mass tensor decreases and fluctuates less when the pairing strength is decreased. The systematic behavior of the  $\eta > 0.5$  pairing force resembles that of increasing the strength of the pairing force.

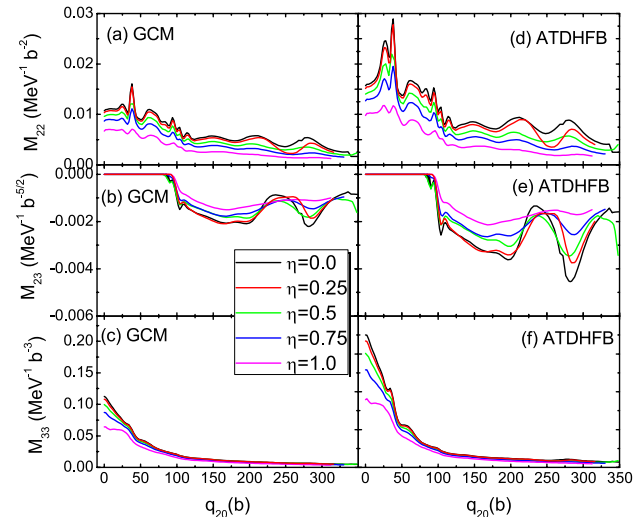


**Fig. 6** (Color online)  $M_{22}$  (top panel),  $M_{23}$  (middle panel), and  $M_{33}$  (bottom panel) of the mass tensors are shown as the elongated deformations along the static fission path for different  $\eta$  values. The results in the left column are obtained by using GCM method, and those in the right column are derived by the ATDHFB method

### 3.4 Scission lines

Determining the scission frontier is critical for describing the fission dynamics. In DFT, the operator  $q_N = \langle \hat{Q}_N \rangle = \left\langle e^{-\left(\frac{z-z_N}{a_N}\right)^2} \right\rangle$  is often used to evaluate the neck size of the fissioning nuclei.  $a_N = 1$  fm is often chosen.  $z_N$  is the neck position, which has the lowest density between the two fragments. Generally, the neck size smoothly decreases as the fissioning nucleus elongates, and decreases to nearly zero after the scission, where the two fragments are sufficiently separated. In this study, we chose  $q_N = 4$  as the critical value for determining the scission line in  $^{240}\text{Pu}$ , which has been used for  $^{240}\text{Pu}$  in Refs. [28, 40]. This value was chosen at the edge of the sudden decrease in the neck size, maintaining most of the pre-fission configurations for further fission dynamic calculations. The scission lines in the PES of the  $(q_{20}, q_{30})$  collective spaces obtained by DFT using the different types of pairing forces are shown in Fig. 7. Generally, the scission contours of the different  $\eta$  values display similar patterns. For different  $\eta$  values, in or around the region of the symmetric fission, the increase of  $\eta$  leads to a smaller quadrupole moment at the scission point. Considering  $\eta = 1.0$ , symmetric fission occurred at the quadrupole moment  $q_{20} \sim 480$  b for  $\eta = 1.0$ , and at approximately 550 b for the other  $\eta$  values. The shortest elongation occurred at  $q_{20} \sim 300$  b when the asymmetry increased to the octupole moment  $q_{30} \sim 30$  b $^{3/2}$ . Subsequently, the scission lines turned toward the upper-right direction until significant

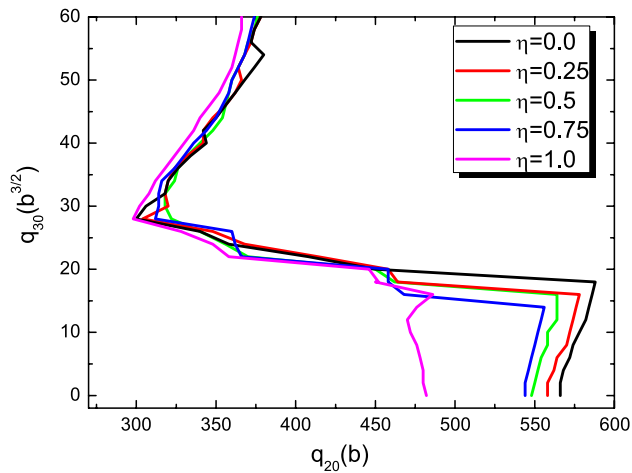


**Fig. 7** (color online) The scission lines using the criterion of  $q_N = 4$  are shown for the different  $\eta$  values

asymmetry appeared. The pre-fission region for  $\eta = 1$  is explicitly smaller than the other cases.

### 3.5 Total kinetic energy

An important quantity in induced fission is the total kinetic energy (TKE), which is obtained by the fission fragments. In this study, the total kinetic energy of the two separated fragments at the scission point can be estimated as the Coulomb repulsive interaction  $E_{\text{TKE}} = \frac{e^2 Z_H Z_L}{d_{\text{ch}}}$ , where  $e$  indicates the proton charge,  $Z_H$  and  $Z_L$  denote the charge number of the heavy and light fragments, respectively, and  $d_{\text{ch}}$  is the relative distance between the centers of charge of the two fragments at the scission point. This approximation for TKE has been frequently used for simplification, as demonstrated in Refs. [15, 20, 22, 57–59]. However, it neglects the dissipation and shell effects, among others, which can lead to an overestimated TKE compared to the experimental data [15, 20, 22, 57–59]. The dissipation effect has been recently considered [60]; thus, the calculated TKE can better agree with the data. The TKE values of the  $^{240}\text{Pu}$  fission fragments with different types of pairing forces were plotted as functions of the heavy fragment mass, as shown in Fig. 8. The open circles represent the calculated results for different  $\eta$  values, whereas the solid circles indicate the experimental data from the thermal neutron-induced  $^{239}\text{Pu}$  fission experiments [61–63]. Considering the general trend, a qualitative dip is reproduced for all types of pairing forces at  $A_H = 120$ , as well as a peak at  $A_H = 134$ . Near the dip or peak, the TKE is larger for larger  $\eta$  values. For  $A_H > 144$ , the discrepancies are fairly small for different pairing forces.

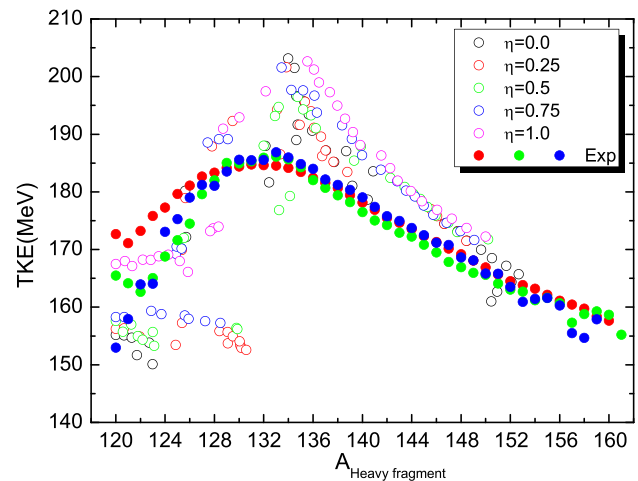


**Fig. 8** (color online) Total kinetic energies of the nascent fission fragments as functions of the heavy fragment mass for  $^{240}\text{Pu}$  based on the different  $\eta$  values. Open symbols represent the calculated results, and solid symbols indicate the experimental data [61–63] for the thermal neutron

### 3.6 Fission yields

Figure 9 presents the mass and charge yields obtained with the code FELIX (version 2) [47] based on the TDGCM+GOA framework using the different types of pairing forces, which are compared with the experimental data. As a critical microscopic input of fission dynamic calculations, the mass tensor is calculated by the GCM or

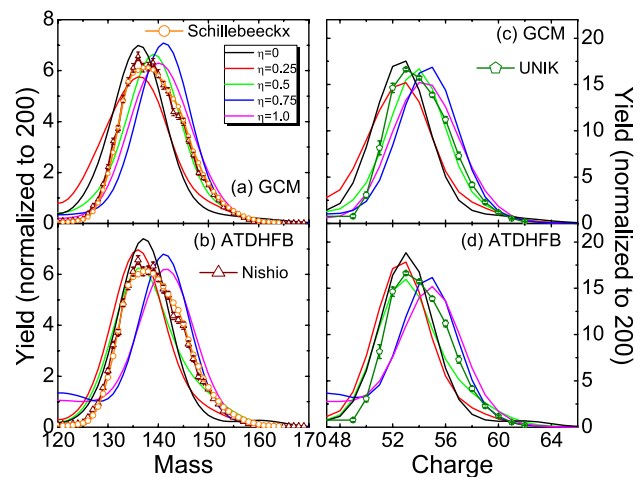


**Fig. 9** (color online) Calculated pre-neutron mass yields [panels a and b] and charge yields [panels c and d] are compared with the experimental data. Only the heavy fragments are displayed. In panels a and c, the mass tensor from the GCM method is used, and in panels b and d, the mass tensor is calculated using the ATDHFB method. Data for the pre-neutron mass yields were obtained from Refs. [64, 65], and those of the charge yield were obtained from Ref. [66]

ATDHFB methods. In this calculation,  $q_N = 4$  was used to determine the scission line. Generally, the discrepancies between the calculated pre-neutron mass distribution and charge distributions obtained by using the mass tensors by the GCM and ATDHFB methods are small. Furthermore, the mass and charge yields calculated by using the mixed pairing force with  $\eta = 0.5$  combined with the mass tensor by the ATDHFB method demonstrated the best agreement with the experimental data.

The impact of the different types of pairing forces on the mass and charge distributions is apparent. For the calculated results obtained by the ATDHFB mass tensor, the position of the peak was nearly constant for  $\eta = 0.0, 0.25,$  and  $0.5,$  and moved toward the heavy fragment as  $\eta = 0.75$  and  $1.0.$  For the results with GCM mass tensor, the mass and charge distributions of the fission fragment shifted toward the more heavy fragment as  $\eta$  increased (panels (a) and (c)). Furthermore, the theoretical calculations obtained by the TDGCM with ATDHFB mass tensors (panels (b) and (d)) demonstrated that the yields from the symmetric fission channel increased as  $\eta$  increased, which was related to the decrease in the height of the ridge as  $\eta$  increased, as shown in Fig. 2.

## 4 Summary

In this study, we focused on analyzing the influence of different types of pairing forces on the fission properties in the framework of SkM\*-DFT and TDGCM+GOA, considering the  $^{239}\text{Pu}(n, f)$  reaction as an example. Different types of pairing interactions were considered in the HFB approximation. The  $\eta$  parameter was tuned to obtain the different types of pairing forces and to test the sensitivity of the calculations.  $\eta = 0, 0.5,$  and  $1.0$  are referred to as the volume-, surface-, and mixed-type pairing forces in the literature, respectively; we also used  $\eta = 0.25$  and  $0.75$  for test purposes.

The PES, mass tensor, scission line, and TKE were calculated. The results demonstrated a significant sensitivity of the fission process to the choice of the  $\eta$ . An increase in the  $\eta$  value led to lower ground-state and isomeric-state energies, as well as fission barriers. Considering surface pairing ( $\eta = 1$ ), the calculated outer barrier was lower than the empirical value. Therefore, it may not be a good choice for the fission study. The strength of these pairing forces was fixed by producing the empirical pairing gaps at the ground states. However, for the large deformations, the pairing force with larger  $\eta$  values tended to have larger pairing gaps. The collective mass tensor decreased and fluctuated less against the deformation with larger  $\eta$  values of the pairing force. For the study of the scission lines, the pre-fission region decreased with larger  $\eta$  values, especially at the region around the symmetric fission channel. The TKE tended to be larger for larger  $\eta$  around the symmetric fission channel,

and around the peak of the TKE distribution. Considering the asymmetric fission region, the TKEs obtained by using the different pairing forces were fairly similar. For the calculation of the fission yields, when the mixed pairing force ( $\eta = 0.5$ ) was used, the results were best-aligned with the data. The peaks of the mass and charge distributions of the fission fragments shifted toward the more heavy fragments as  $\eta$  increased. When the ATDHFB mass tensor was used, a small peak in the symmetric fission channel appeared for  $\eta = 0.75$  and  $1,$  which contradicts with the experimental data.

**Author contributions** All authors contributed to the study conception and design. Material preparation, data collection, and analysis were performed by YS, YJC, ZYL, LLL, GXD, and XBW. The first draft of the manuscript was written by YS, and all authors commented on previous versions of the manuscript. All authors read and approved the final manuscript.

**Data availability statement** The data that support the findings of this study are openly available in Science Data Bank at <https://cstr.cn/31253.11.sciencedb.16295> and <https://doi.org/10.57760/sciencedb.16295>

## Declarations

**Conflict of interest** The authors declare that they have no Conflict of interest.

## References

1. L. Meitner, O.R. Frisch, Disintegration of uranium by neutrons: a new type of nuclear reaction. *Nature (London)* **143**, 239 (1939). <https://doi.org/10.1038/143239a0>
2. O. Hahn, F. Strassmann, Über den Nachweis und das Verhalten der bei der Bestrahlung des Urans mittels Neutronen entstehenden Erdalkalimetalle. *Naturwissenschaften* **27**, 11 (1939). <https://doi.org/10.1007/BF01488241>
3. J. Krappe, K. Pomorski, *Theory of nuclear fission* (Springer-Verlag, Berlin, Heidelberg (2012)). <https://doi.org/10.1007/978-3-642-23515-3>
4. J.H. Hamilton, S. Hofmann, Y.T. Oganessian, Search for super-heavy nuclei. *Annu. Rev. Nucl. Part. Sci.* **63**, 383 (2013). <https://doi.org/10.1146/annurev-nucl-102912-144535>
5. J.C. Pei, W. Nazarewicz, J.A. Sheikh et al., Fission barriers of compound superheavy nuclei. *Phys. Rev. Lett.* **102**, 192501 (2009). <https://doi.org/10.1103/PhysRevLett.102.192501>
6. A. Baran, M. Kowal, P.G. Reinhard et al., Fission barriers and probabilities of spontaneous fission for elements with  $Z \geq 100$ . *Nucl. Phys. A* **944**, 442 (2015). <https://doi.org/10.1016/j.nuclphysa.2015.06.002>
7. S. Goriely, J.L. Sida, J.F. Lemaître et al., New fission fragment distributions and  $r$ -process origin of the rare-earth elements. *Phys. Rev. Lett.* **111**, 242502 (2013). <https://doi.org/10.1103/PhysRevLett.111.242502>
8. N. Schunck, L.M. Robledo, Microscopic theory of nuclear fission: a review. *Rep. Prog. Phys.* **79**, 116301 (2016). <https://doi.org/10.1088/0034-4885/79/11/116301>
9. K.H. Schmidt, B. Jurado, Review on the progress in nuclear fission-experimental methods and theoretical descriptions. *Rep. Prog. Phys.* **81**, 106301 (2018). <https://doi.org/10.1088/1361-6633/aacfa7>

10. M. Bender, R. Bernard, G. Bertsch et al., Future of nuclear fission theory. *J. Phys. G* **47**, 113002 (2020). <https://doi.org/10.1088/1361-6471/abab4f>
11. Q.F. Song, L. Zhu, H. Guo et al., Verification of neutron-induced fission product yields evaluated by a tensor decomposition model in transport-burnup simulations. *Nucl. Sci. Tech.* **34**, 32 (2023). <https://doi.org/10.1007/s41365-023-01176-5>
12. Z.X. Fang, M. Yu, Y.G. Huang et al., Theoretical analysis of long-lived radioactive waste in pressurized water reactor. *Nucl. Sci. Tech* **32**, 72 (2021). <https://doi.org/10.1007/s41365-021-00911-0>
13. Y. Qiang, J.C. Pei, Energy and pairing dependence of dissipation in real-time fission dynamics. *Phys. Rev. C* **104**, 054604 (2021). <https://doi.org/10.1103/PhysRevC.104.054604>
14. M.H. Zhou, Z.Y. Li, S.Y. Chen et al., Three-dimensional potential energy surface for fission of  $^{236}\text{U}$  within covariant density functional theory. *Chin. Phys. C* **47**, 064106 (2023). <https://doi.org/10.1088/1674-1137/acc4ac>
15. Z.X. Ren, J. Zhao, D. Vretenar et al., Microscopic analysis of induced nuclear fission dynamics. *Phys. Rev. C* **105**, 044313 (2022). <https://doi.org/10.1103/PhysRevC.105.044313>
16. L.L. Liu, X.Z. Wu, Y.J. Chen et al., Study of fission dynamics with a three-dimensional Langevin approach. *Phys. Rev. C* **99**, 044614 (2019). <https://doi.org/10.1103/PhysRevC.99.044614>
17. L.L. Liu, X.Z. Wu, Y.J. Chen et al., Impact of nuclear dissipation on the fission dynamics within the Langevin approach. *Phys. Rev. C* **105**, 034614 (2022). <https://doi.org/10.1103/PhysRevC.105.034614>
18. S.A. Giuliani, L.M. Robledo, Fission properties of the Barcelona-Catania-Paris-Madrid energy density functional. *Phys. Rev. C* **88**, 054325 (2013). <https://doi.org/10.1103/PhysRevC.88.054325>
19. N. Schunck, D. Duke, H. Carr et al., Description of induced nuclear fission with Skyrme energy functionals: Static potential energy surfaces and fission fragment properties. *Phys. Rev. C* **90**, 054305 (2014). <https://doi.org/10.1103/PhysRevC.90.054305>
20. H. Tao, J. Zhao, Z.P. Li et al., Microscopic study of induced fission dynamics of  $^{226}\text{Th}$  with covariant energy density functionals. *Phys. Rev. C* **96**, 024319 (2017). <https://doi.org/10.1103/PhysRevC.96.024319>
21. S. Karatzikos, A.V. Afanasjev, G.A. Lalazissis et al., The fission barriers in Actinides and superheavy nuclei in covariant density functional theory. *Phys. Lett. B* **689**, 72 (2010). <https://doi.org/10.1016/j.physletb.2010.04.045>
22. Y.J. Chen, Y. Su, G.X. Dong et al., Energy density functional analysis of the fission properties of  $^{240}\text{Pu}$ : The effect of pairing correlations. *Chin. Phys. C* **46**, 024103 (2022). <https://doi.org/10.1088/1674-1137/ac347a>
23. J. Zhao, T. Nikšić, D. Vretenar et al., Time-dependent generator coordinate method study of fission: mass parameters. *Phys. Rev. C* **101**, 064605 (2020). <https://doi.org/10.1103/PhysRevC.101.064605>
24. A. Bulgac, S. Jin, K.J. Roche et al., Fission dynamics of  $^{240}\text{Pu}$  from saddle to scission and beyond. *Phys. Rev. C* **100**, 034615 (2019). <https://doi.org/10.1103/PhysRevC.100.034615>
25. Y. Qiang, J.C. Pei, P.D. Stevenson, Fission dynamics of compound nuclei: pairing versus fluctuations. *Phys. Rev. C* **103**, L031304 (2021). <https://doi.org/10.1103/PhysRevC.103.L031304>
26. J. Zhao, T. Nikšić, D. Vretenar, Microscopic self-consistent description of induced fission: dynamical pairing degree of freedom. *Phys. Rev. C* **104**, 044612 (2021). <https://doi.org/10.1103/PhysRevC.104.044612>
27. X. Guan, J.H. Zheng, M.Y. Zheng, Pairing effects on the fragment mass distribution of Th, U, Pu, and Cm isotopes. *Nucl. Sci. Tech.* **34**, 173 (2023). <https://doi.org/10.1007/s41365-023-01316-x>
28. X.B. Wang, Y.J. Chen, G.X. Dong et al., Role of pairing correlations in the fission process. *Phys. Rev. C* **108**, 034306 (2023). <https://doi.org/10.1103/PhysRevC.108.034306>
29. X. Guan, T.C. Wang, W.Q. Jiang et al., Impact of the pairing interaction on fission of U isotopes. *Phys. Rev. C* **107**, 034307 (2023). <https://doi.org/10.1103/PhysRevC.107.034307>
30. R.R. Chasman, Density-dependent delta interactions and actinide pairing matrix elements. *Phys. Rev. C* **14**, 1935 (1976). <https://doi.org/10.1103/PhysRevC.14.1935>
31. S.A. Fayans, S.V. Tolokonnikov, E.L. Trykov et al., Isotope shifts within the energy-density functional approach with density dependent pairing. *Phys. Lett. B* **338**, 1 (1994). [https://doi.org/10.1016/0370-2693\(94\)91334-X](https://doi.org/10.1016/0370-2693(94)91334-X)
32. J. Dobaczewski, W. Nazarewicz, T.R. Werner et al., Mean-field description of ground-state properties of drip-line nuclei: pairing and continuum effects. *Phys. Rev. C* **53**, 2809 (1996). <https://doi.org/10.1103/PhysRevC.53.2809>
33. J. Dobaczewski, W. Nazarewicz, T.R. Werner, Closed shells at drip-line nuclei. *Phys. Scr. T* **56**, 15 (1995). <https://doi.org/10.1088/0031-8949/1995/T56/002>
34. S.A. Changizi, C. Qi, Density dependence of the pairing interaction and pairing correlation in unstable nuclei. *Phys. Rev. C* **91**, 024305 (2015). <https://doi.org/10.1103/PhysRevC.91.024305>
35. H.Q. Shi, X.B. Wang, G.X. Dong et al., Abnormal odd-even staggering behavior around  $^{132}\text{Sn}$  studied by density functional theory. *Chin. Phys. C* **44**, 094108 (2020). <https://doi.org/10.1088/1674-1137/44/9/094108>
36. J. Dobaczewski, W. Nazarewicz, M.V. Stoitsov, Nuclear ground-state properties from mean-field calculations. *Eur. Phys. J. A* **15**, 21 (2002). <https://doi.org/10.1140/epja/i2001-10218-8>
37. M. Bender, P.H. Heenen, P.G. Reinhard, Self-consistent mean-field models for nuclear structure. *Rev. Mod. Phys.* **75**, 121 (2003). <https://doi.org/10.1103/RevModPhys.75.121>
38. J.F. Berger, M. Girod, D. Gogny, Time-dependent quantum collective dynamics applied to nuclear fission. *Comput. Phys. Commun.* **63**, 365 (1991). [https://doi.org/10.1016/0010-4655\(91\)90263-K](https://doi.org/10.1016/0010-4655(91)90263-K)
39. R. Bernard, H. Goutte, D. Gogny et al., Microscopic and nonadiabatic Schrödinger equation derived from the generator coordinate method based on zero- and two-quasiparticle states. *Phys. Rev. C* **84**, 044308 (2011). <https://doi.org/10.1103/PhysRevC.84.044308>
40. D. Regnier, N. Dubray, N. Schunck et al., Fission fragment charge and mass distributions in  $^{239}\text{Pu}(n, f)$  in the adiabatic nuclear energy density functional theory. *Phys. Rev. C* **93**, 054611 (2016). <https://doi.org/10.1103/PhysRevC.93.054611>
41. E. Perlińska, S.G. Rohoziński, J. Dobaczewski et al., Local density approximation for proton-neutron pairing correlations: formalism. *Phys. Rev. C* **69**, 014316 (2004). <https://doi.org/10.1103/PhysRevC.69.014316>
42. J. Dobaczewski, J. Dudek, Time-odd components in the mean-field of rotating superdeformed nuclei. *Phys. Rev. C* **52**, 1827 (1995). <https://doi.org/10.1103/PhysRevC.52.1827>
43. W.J. Chen, C.A. Bertulani, F.R. Xu et al., Odd-even mass staggering with Skyrme–Hartree–Fock–Bogoliubov theory. *Phys. Rev. C* **91**, 047303 (2015). <https://doi.org/10.1103/PhysRevC.91.047303>
44. J. Dobaczewski, W. Nazarewicz, P.G. Reinhard, Pairing interaction and self-consistent densities in neutron-rich nuclei. *Nucl. Phys. A* **693**, 361 (2001). [https://doi.org/10.1016/S0375-9474\(01\)00993-9](https://doi.org/10.1016/S0375-9474(01)00993-9)
45. N. Tajima, P. Bonche, H. Flocard et al., Self-consistent calculation of charge radii of Pb isotopes. *Nucl. Phys. A* **551**, 434 (1993). [https://doi.org/10.1016/0375-9474\(93\)90456-8](https://doi.org/10.1016/0375-9474(93)90456-8)
46. J. Terasaki, P.H. Heenen, P. Bonche et al., 3D solution of Hartree–Fock–Bogoliubov equations for drip-line nuclei. *Nucl. Phys. A* **593**, 1 (1995). [https://doi.org/10.1016/0375-9474\(96\)00036-X](https://doi.org/10.1016/0375-9474(96)00036-X)
47. D. Regnier, N. Dubray, M. Verriere et al., FELIX-2.0: New version of the finite element solver for the time dependent generator coordinate method with the Gaussian overlap approximation. *Comput. Phys. Commun.* **225**, 180 (2018). <https://doi.org/10.1016/j.cpc.2017.12.007>

48. J. Bartel, P. Quentin, M. Brack et al., Towards a better parametrisation of Skyrme-like effective forces: a critical study of the SkM force. *Nucl. Phys. A* **386**, 79 (1982). [https://doi.org/10.1016/0375-9474\(82\)90403-1](https://doi.org/10.1016/0375-9474(82)90403-1)
49. R. Navarro Perez, N. Schunck, R.D. Lasserri et al., Axially deformed solution of the Skyrme–Hartree–Fock–Bogolyubov equations using the transformed harmonic oscillator basis (III) hfbtho (v3.00): A new version of the program. *Comput. Phys. Commun.* **220**, 363 (2017). <https://doi.org/10.1016/j.cpc.2017.06.022>
50. M. Bender, K. Rutz, P.-G. Reinhard et al., Pairing gaps from nuclear mean-field models. *Eur. Phys. J. A* **8**, 59–75 (2000). <https://doi.org/10.1007/s10050-000-4504-z>
51. G.F. Bertsch, C.A. Bertulani, W. Nazarewicz et al., Odd-even mass differences from self-consistent mean-field theory. *Phys. Rev. C* **79**, 034306 (2009). <https://doi.org/10.1103/PhysRevC.79.034306>
52. B.N. Lu, J. Zhao, E.G. Zhao et al., Multidimensionally-constrained relativistic mean-field models and potential-energy surfaces of actinide nuclei. *Phys. Rev. C* **89**, 014323 (2014). <https://doi.org/10.1103/PhysRevC.89.014323>
53. L. Chen, C. Zhou, Y. Shi, Fission barriers of actinide nuclei with nuclear density functional theory: influence of the triaxial deformation. *Eur. Phys. J. A* **56**, 180 (2020). <https://doi.org/10.1140/epja/s10050-020-00182-0>
54. M. Wang, W.J. Huang, F.G. Kondev et al., The AME 2020 atomic mass evaluation (II). Tables, graphs and references. *Chin. Phys. C* **45**, 030003 (2021). <https://doi.org/10.1088/1674-1137/abddaf>
55. B. Singh, R. Zywina, R. B. Firestone, Table of superdeformed nuclear bands and fission isomers: third edition (October 2002). *Nucl. Data Sheets* **97**, 241 (2002). <https://doi.org/10.1006/ndsh.2002.0018>
56. R. Capote, M. Herman, P. Oblozinsky et al., RIPL-reference input parameter library for calculation of nuclear reactions and nuclear data evaluations. *Nucl. Data Sheets* **110**, 3107 (2009). <https://doi.org/10.1016/j.nds.2009.10.004>
57. H. Goutte, J.F. Berger, P. Casoli et al., Microscopic approach of fission dynamics applied to fragment kinetic energy and mass distributions in  $^{238}\text{U}$ . *Phys. Rev. C* **71**, 024316 (2005). <https://doi.org/10.1103/PhysRevC.71.024316>
58. Z.Y. Li, S.Y. Chen, Y.J. Chen et al., Microscopic study on asymmetric fission dynamics of  $^{180}\text{Hg}$  within covariant density functional theory. *Phys. Rev. C* **106**, 024307 (2022). <https://doi.org/10.1103/PhysRevC.106.024307>
59. Y.J. Chen, Y. Su, L.L. Liu et al., Microscopic study of neutron-induced fission process of  $^{239}\text{Pu}$  via zero- and finite-temperature density functional theory. *Chin. Phys. C* **47**, 054103 (2023). <https://doi.org/10.1088/1674-1137/acbe2c>
60. J. Zhao, T. Nikšić, D. Vretenar, Time-dependent generator coordinate method study of fission. II. Total kinetic energy distribution. *Phys. Rev. C* **106**, 054609 (2022). <https://doi.org/10.1103/PhysRevC.106.054609>
61. V.M. Surin, A.I. Sergachev, N.I. Rezhnikov et al., Yields and kinetic energies of fragments in the Fission of  $^{233}\text{U}$  and  $^{240}\text{Pu}$  by 5.5- and 15-MeV Neutrons. *Soviet J. Nucl. Phys.* **14**, 523 (1972)
62. C. Wagemans, E. Allaert, A. Deruytter et al., Comparison of the energy and mass characteristics of the  $^{239}\text{Pu}$  ( $n_{\text{th}}$ , f) and the  $^{239}\text{Pu}$ (sf) fragments. *Phys. Rev. C* **30**, 218 (1984). <https://doi.org/10.1103/PhysRevC.30.218>
63. P. Geltenbort, F. Goennenwein, A. Oed, Precision measurements of mean kinetic energy release in thermal-neutron-induced fission of  $^{233}\text{U}$ ,  $^{235}\text{U}$  and  $^{239}\text{Pu}$ . *Conf. Nucl. Data Basic Appl. Sci., Santa Fe 1985*, Vol.1, p.393 (1985), USA
64. P. Schillebeeckx, C. Wagemans, A.J. Deruytter et al., Comparative study of the fragments' mass and energy characteristics in the spontaneous fission of  $^{238}\text{Pu}$ ,  $^{240}\text{Pu}$  and  $^{242}\text{Pu}$  and in the thermal-neutron-induced fission of  $^{239}\text{Pu}$ . *Nucl. Phys. A* **545**, 623 (1992). [https://doi.org/10.1016/0375-9474\(92\)90296-V](https://doi.org/10.1016/0375-9474(92)90296-V)
65. K. Nishio, Y. Nakagome, I. Kanno et al., Measurement of fragment mass dependent kinetic energy and neutron multiplicity for thermal neutron induced fission of plutonium-239. *J. Nucl. Sci. Technol.* **32**, 404 (1995). <https://doi.org/10.1080/18811248.1995.9731725>
66. W. Reisdorf, J.P. Unik, H.C. Griffin et al., Fission fragment K x-ray emission and nuclear charge distribution for thermal neutron fission of  $^{233}\text{U}$ ,  $^{235}\text{U}$ ,  $^{239}\text{Pu}$  and spontaneous fission of  $^{252}\text{Cf}$ . *Nucl. Phys. A* **177**, 33 (1971). [https://doi.org/10.1016/0375-9474\(71\)90297-1](https://doi.org/10.1016/0375-9474(71)90297-1)

Springer Nature or its licensor (e.g. a society or other partner) holds exclusive rights to this article under a publishing agreement with the author(s) or other rightsholder(s); author self-archiving of the accepted manuscript version of this article is solely governed by the terms of such publishing agreement and applicable law.